A universal zigzag edge reconstruction of α-phase puckered monolayer and its resulting robust charge spatial separation

Yanxue Zhang[1], Yanyan Zhao[1], Yizhen Bai[1], Junfeng Gao[1*], Jijun Zhao[1], Yong-Wei Zhang[2*]

1. Key laboratory of Materials Modification by Laser, Ion and Electron Beams (Dalian University of Technology), Ministry of Education, Dalian, 116024, China

2. Institute of High Performance Computing, A*STAR, 138632 Singapore

Junfeng Gao (gaojf@dlut.edu.cn), Yong-Wei Zhang (zhangyw@ihpc.a-star.edu.sg)

Abstract: Edge is important as it dictates the stability and properties of nanoribbons. Here, we reveal a universal reconstruction of ZZ edge into (2×1) tubed [ZZ(Tube)] edge, enabling ultimate narrow nanotube to terminate nanoribbons, for α-puckered group-V elemental and compound monolayers (GeS/Se and SnS/Se). The reconstructed edge formations are confirmed by CALYPSO. The ZZ(Tube) edge is easy to form, highly stable, and semiconducting. Remarkably, ZZ(Tube) edge always exhibits a type-II band structure, and a robust VBM and CBM charge spatial separation. For a compound monolayer monochalcogenide, mild (2×1) ZZ(S-R) occurs at the chalcogenide-terminated edge. TDDFT simulations indicate that the charge separation occurs only in 672 fs, while the life time is over 5 ns, thus facilitating robust spatial charge accumulation. These remarkable features of ZZ(Tube) edge-terminated α-puckered nanoribbons are ideal for optoelectronic and photocatalytic applications.

Keywords: Edge reconstruction, α-phase puckered monolayer, zigzag edge, nanotube, charge separation.

Introduction

Different from flat graphene, buckling silicene and sandwiched structural MoS_2, two dimensional (2D) α-phase monolayers, such as, black phosphorene, arsenene and monochalcogenide (GeS/Se and SnS/Se) have a unique puckered structure.[1-3] Since they have a high anisotropy in both electronic and optical properties,[4-6] these materials are promising for applications in thermoelectricity,[7-10] piezoelectricity,[11-13] ferroelectricity[14-16] etc. Besides, these materials usually possess a considerably high carrier mobility (10^3 $cm^2V^{-1}s^{-1}$)[17-21], and a suitable band gap (1.44~2.32 eV for monolayer)[6,22], which are tunable by changing thickness, or applying electric field and strain[20,23-26]. Therefore, they are often considered as excellent candidates for applications in ultra-fast micro-electronics, photo-electronics and photo-catalyst.[19,27-33]

Edge, which breaks the continuity of 2D materials, is inevitable in real devices. Due to the presence of dangling bonds, local states or edge stress, edge often influences the stability of 2D materials, especially at the nanoscale.[34,35] Among all the different edges, zigzag (ZZ) edge in honeycomb-like lattice is most likely to reconstruct because dangling bonds at ZZ edge are hard to be self-passivated.[36-40] For example, ZZ edge of graphene reconstructs into ZZ(57) edge, reducing the edge energy and releasing edge stress.[36,41-46] For ZZ edge of sandwiched TMDs, Cui et al. predicted unique (2×1) reconstruction for M edge and (2×1) and (3×1) for X edge (M = Mo, W; X = S, Se), respectively.[39,47]

Beyond reducing the edge energy, edge reconstruction can also dramatically alter the electronic properties of nanoribbons. For instance, ZZ(57) edge removes dangling bonds, which changes the half-metal properties of ZZ edge graphene.[36,48] Recently, a nanotube edge reconstruction of black phosphorene was proposed by several groups.[38,49,50] Such tube reconstruction enables a small nanotube to terminate a phosphorene nanoribbon (PNR), reducing 35% edge energy.[38] Moreover, the unique edge reconstruction transforms the electronic properties of phosphorene with zigzag edge from metallic to semiconducting with a gap of 1.23 eV.[38] In addition, the edge reconstruction also alters the vibrational modes of PNR, and changes its thermal conductivity.[51]

Arsenene and monochalcogenide (GeS/Se and SnS/Se) resemble α-phase of black phosphorene.[22,52] It is expected that their ZZ edges may also undergo a similar edge reconstruction. However, monochalcogenides (GeS/Se and SnS/Se) are a binary compound. It is also expected that their edge reconstruction may be different from phosphorene. To our best knowledge, all existing studies only focus on the pristine edges of monolayer monochalcogenide nanoribbons.[53] Therefore, the edge reconstruction in monochalcogenides and its influences on the edge stability and physical properties are still interesting and important topics.

In this letter, we first show that the tube edge is a universal reconstruction for ZZ edge in α-phase puckered monolayers, such as group-V arsenene and group-IV monochalcogenide (GeS/Se and SnS/Se), by using first-principles and CALYPSO calculations. For elemental arsenene nanoribbon (ANR), tube edge reconstruction occurs at both sides. In contrast, two types of reconstruction for the ZZ metal and chalcogens edges exist for monochalcogenide. Take GeS as an example, ZZ(Ge-Tube) is the global ground state along ZZ metal edge, while a mild edge (2×1) ZZ(S-R) is the most stable S edge. The reconstruction barriers for ZZ(Ge-Tube) and ZZ(S-R) edges are as low as 0.41 eV and 0.016 eV, separately. We further verify their dynamic stability by the AIMD simulations. Beyond, the reconstructed edge is against hydrogenation even under elevated temperature and high hydrogen partial pressures. In addition, we would like to emphasize that the ZZ(Tube) edge always induces a type-II semiconducting band alignment, and a robust charge spatial separation. Remarkably, our time-dependent density functional theory (TDDFT) simulations predict a charge separation time of 672 fs, which is much shorter than the life time (5 ns), indicating that the separated charges can be effectively accumulated, which is crucial for the applications in optoelectronics and photocatalysis.

1. Edge reconstruction structure

We first compare the edge energy of pristine ZZ(Pri) and ZZ(Tube) edges of puckered group-V ANR (~35 Å) (Figure S1a). The edge energy of ZZ(Pri) is 1.9 eV/nm, in good agreement with previous results.[25] In contrast, the edge energy of reconstructed ZZ(Tube) edge is only 1.0 eV/nm, a 47% lower than the pristine counterpart. The ZZ(Tube) edge is even more stable than the previously predicted ZZRC-o edge (1.5 eV/nm).[25] The structure and energy gain of the tube reconstruction of ZZ arsenene are very similar to that of ZZ phosphorene. Therefore, we conclude tube reconstruction is a common phenomenon for elemental puckered monolayers.

Next, we explore the ZZ edge of puckered α-phase monochalcogenide monolayer. Take GeS as an example, GeS possesses two types of zigzag edge, that is, metal Ge edge and nonmetal S edge. The edge reconstruction of compound GeS is expected to be more complex. Therefore, we resort to CALYPSO,[54-56] a well-known efficient structure searching package, to predict Ge and S edge reconstructions. The schematics of input models are shown in Figure 1a, b. The atoms near edge are fully rearranged by CALYPSO and then relaxed by ab initio calculations, while the inner part far away from the edge is fixed to mimic the intrinsic monolayer structure. We take the tubed structure ZZ(Ge-Tube) as one of the initial seeds.

The search results are plotted in Figure 1e, f after hundreds of individuals being auto built and simulated. We finally obtained two global lowest-energy structures, (2×1) ZZ(Ge-Tube) (Figure 1c) for Ge side and ZZ(S-R) (Figure 1d) for S side of ZZ GeS nanoribbon (GeSNR). The bond length and bond angle details of ZZ(Ge-Tube) edge and ZZ(S-R) edge are shown in Figure S2a,b. Compared with pristine ZZ GeSNR, the reconstructed GeSNR with ZZ(Ge-Tube) and ZZ(S-R) edges reduces the energy by 1.14 eV (Figure 1g). The energy reduction is mainly contributed by ZZ(Ge-Tube) edge, which reduces the energy by 1.04 eV/unit (Figure 1e). The edge reconstruction is also found to reduce the edge stress as the edge reconstruction results in an increase in the equilibrium lattice constant of the GeSNR (Figure S2c).

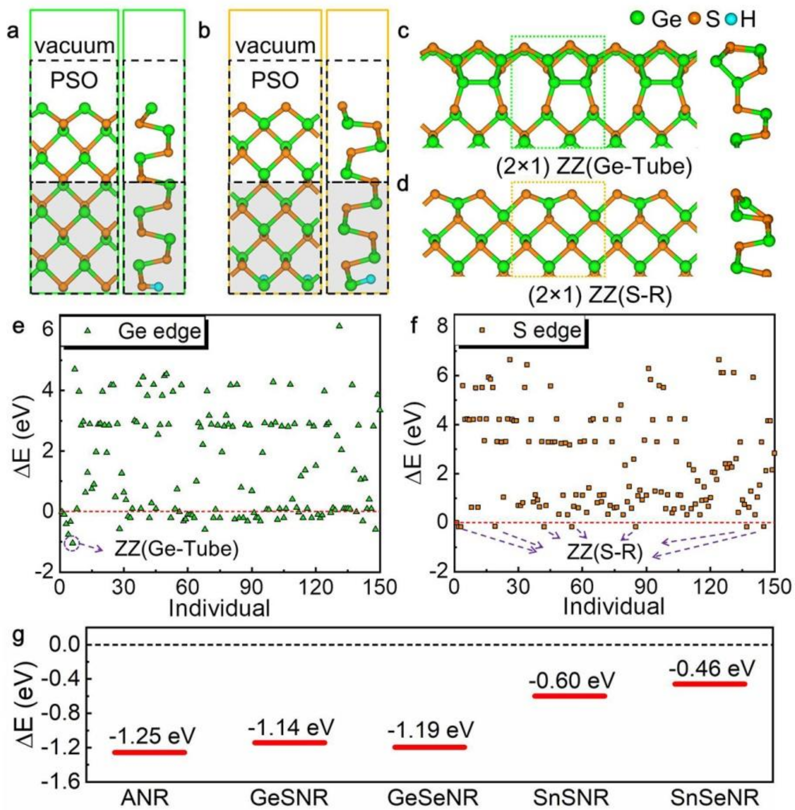

Figure 1. The schematic of CALYPSO input models of (a) Ge edge and (b) S edge of GeSNR, respectively. Atomic structures of lowest-energy (c) ZZ(Ge-Tube) and (d) ZZ(S-R) edge. (e) and (f) are the energy changes (ΔE) of predicted Ge edge and S edge referring to pristine zigzag Ge edge and S edge, respectively. (g) The energies of reconstructed ANR, GeSNR, GeSeNR, SnSNR and SnSeNR compared with the pristine one (dash line set as zero correspondingly).

Subsequently, based on the predicted most stable ZZ(S-R) edge and ZZ(Ge-Tube) edge, we built similar models for puckered GeSeNR, SnSNR and SnSeNR (~33 Å). In Figure 1g, we list the energies of reconstructed ANR, GeSNR, GeSeNR, SnSNR and SnSeNR with reference to their pristine one. Clearly, all edge reconstructions reduce the edge energy significantly. For compound monolayer monochalcogenide, we find that ZZ(Ge-Tube) edge is more stable than ZZ(Sn-Tube) edge. Therefore, ZZ(Tube) is expected to be the universal ZZ edge reconstruction for both elemental and binary puckered α-phase monolayers.

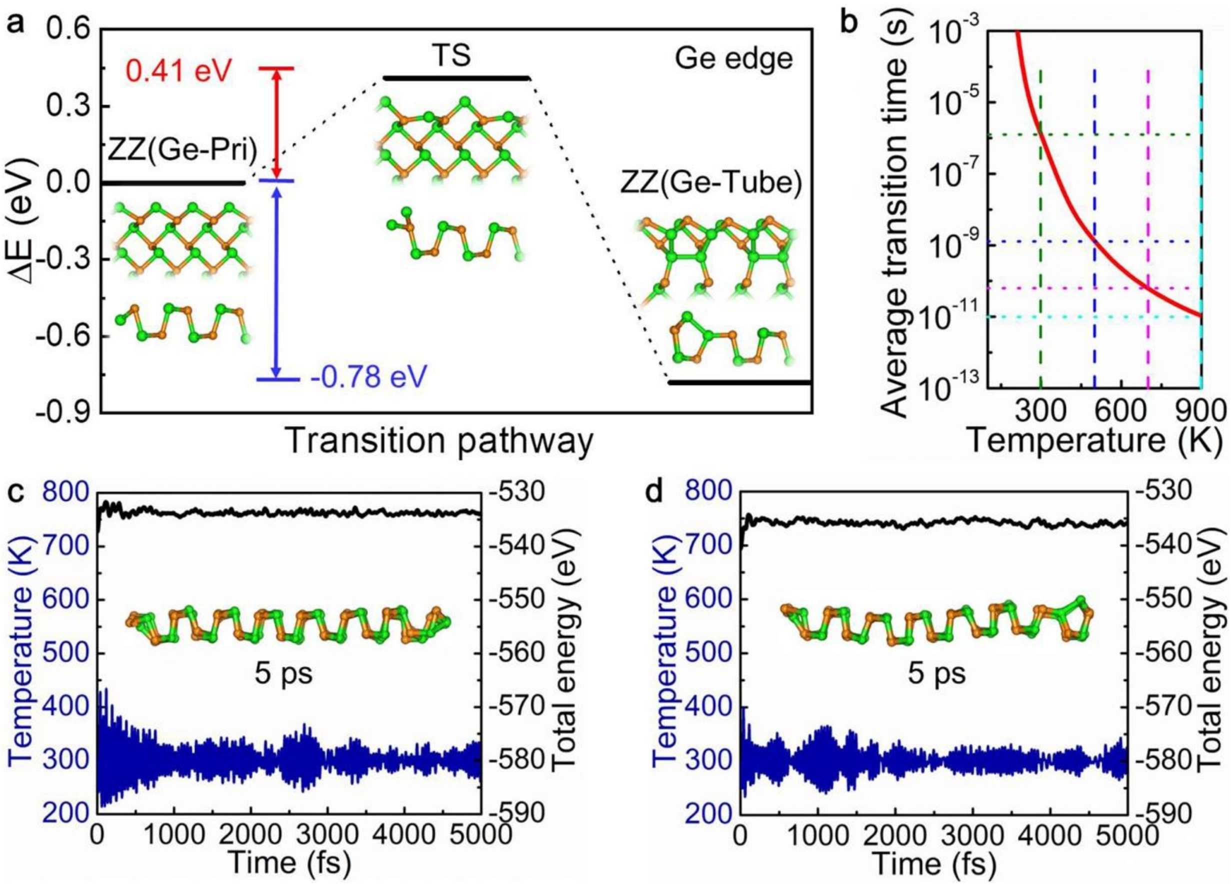

Figure 2. (a) The edge reconstruction process of GeSNR from ZZ(Ge-Pri) edge to ZZ(Ge-Tube) edge and (b) related average transition time under different temperatures. The AIMD simulations at 300 K for (c) pristine and (d) reconstructed GeSNR, respectively. The inset figure in (c, d) is the structure of pristine and reconstructed GeSNR after 5 ps AIMD simulations, respectively.

2. Edge reconstruction process and energy barrier

Next we would like to reveal how these tube reconstructions form. We employed CI-NEB to search for the key transition pathway and barriers of GeS edge reconstructions. As shown in Figure 2a, the obtained transition barrier from ZZ(Ge-Pri) to ZZ(Ge-Tube) edge is just 0.41 eV. We then can assess the average edge transition rate R:

$$\mathrm{R}{\sim}\left(\frac{k_B\mathrm{T}}{h}\right)\times\exp(\text{-}\Delta\mathrm{E}/k_B\mathrm{T}) \qquad (1)$$

where, k_B is the Boltzmann constant. T and h are the temperature and the Plank constant, respectively. ΔE is the energy barrier. The calculated average transition time as a function of temperature is plotted in Figure 2b. The ZZ(Ge-Tube) edge transition rate R reaches 10^5 Hz at 300 K, and 10^7 Hz at 400 K.

Compared to the reconstruction of Ge edge, the transition of S edge from ZZ(S-Pri) to ZZ(S-R) is even easier with a barrier as low as 0.016 eV (Figure S3a). The average transition time is several picoseconds at room temperature (Figure S3b). The kinetic formations of ZZ(Ge-Tube) and ZZ(S-R) are both very easy and fast, thereby, these edge reconstructions should also be very easy and fast.

We further simulated the edge reconstruction of GeSeNR. The kinetic barrier for Ge and Se edge reconstruction is 0.74 eV and 0.013 eV, respectively. The transition barrier of GeSeNR is very close to that of GeSNR, implying that the kinetic behaviors of puckered α-phase compound monochalcogenides are the same.

To confirm the thermal stability of reconstructed GeSNR, we performed AIMD on both pristine (Figure 2c) and reconstructed GeSNR (Figure 2d) at 300 K within NVT ensemble. After 5 ps simulation, the Ge edge of pristine GeSNR deforms significantly with partial Ge-S bonds being broken. Besides, the ZZ(S-R) edge is formed from ZZ(S-Pri) edge spontaneously, agreeing with the analyses of Figure 2b. In contrast, the reconstructed GeSNR is still intact after 5 ps, implying its high structural stability.

3. Thermodynamic phase diagram analysis

Hydrogenation is a very common method to protect 2D edge, such as hydrogenated graphene ZZ edge, hydrogenated phosphorene edge.[7,57] Here, we compared the stability of hydrogenated pristine edge and reconstructed edge. The hydrogenated edge formation energy E_H can be calculated by using: $E_H=\frac{1}{2L}\left(E_{total}-E_{GeSNR}-\frac{N_H}{2}E_{H_2}\right)$, where E_{total}, E_{GeSNR}, and E_{H_2} are the total energies of the hydrogenated GeSNR, bare pristine GeSNR and H_2 molecule, respectively, and N_H is the number of hydrogen atoms adsorbed along the edge.

For a given chemical potential μ_{H_2}, the relative stability of the hydrogenated edge with respect to the bare edge or reconstructed edge can be compared by:[7,58] $G_H=E_H-\frac{\rho_H}{2}\mu_{H_2}$, where $\rho_H=N_H/(2L)$. At temperature T and under partial pressure $P(H_2)$, the chemical potential of H_2 gas is: $\mu_{H_2}=H^0(T)-H^0(0)-TS^0(T)+k_B T\ln\left[\frac{P(H_2)}{P_0}\right]$, where $H^0(0)$ and $S^0(T)$ are obtained from the NIST-JANAF thermochemical tables,[59] and the reference pressure is P_0 = 1 bar.

Then we can calculate the phase diagram of these edges. Among all the explored edges, ZZ(Ge-Tube) edge is highly stable against hydrogenation (Figure 3d). The formation energy E_H of ZZ(Ge-Tube) is a large positive value. Therefore, ZZ(Ge-Tube) can retain without being hydrogenated even under very high H_2 partial pressure (>10^8 bar) at room temperature. While the hydrogenated pressure for other edges is several orders of magnitude lower than ZZ(Ge-Tube). The critical hydrogenated pressure of ZZ(Ge-Pri) (Figure 3c) and ZZ(S-R) (Figure 3b) is close to 10^{-5} bar under room temperature, while ZZ(S-Pri) (Figure 3a) is highly likely to be hydrogenated even under 10^{-6} bar hydrogen partial pressure at 300 K.

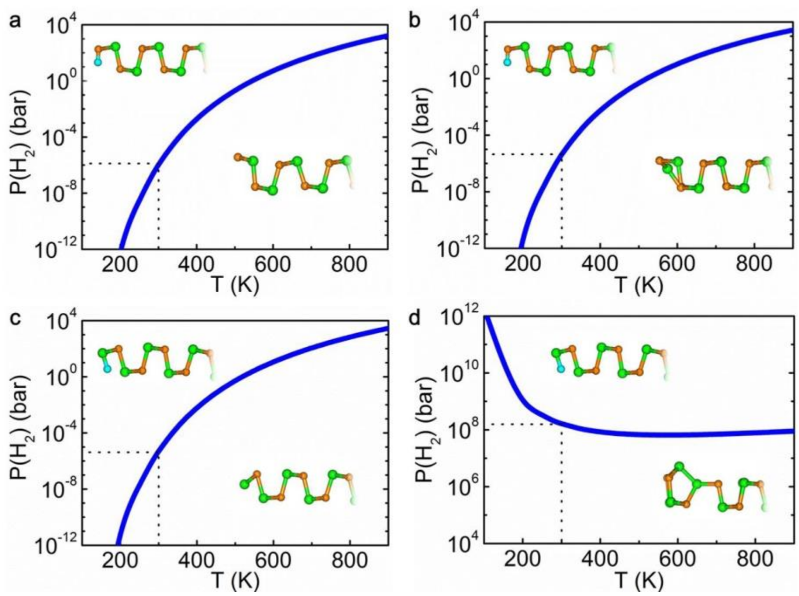

Figure 3. (a) The phase diagram of (a) hydrogenated ZZ(S-Pri) edge versus bare ZZ(S-Pri) edge, (b) hydrogenated ZZ(S-Pri) edge versus bare ZZ(S-R) edge, (c) hydrogenated ZZ(Ge-Pri) edge versus bare ZZ(Ge-Pri) edge and (d) hydrogenated ZZ(Ge-Pri) edge versus bare ZZ(Ge-Tube) edge at various temperatures and partial hydrogen pressures.

So far, we have shown that the ZZ(Tube) reconstruction with low-energy, low transition barrier and ultra-high stability, is the common edge of α-phase elemental and compound monochalcogenide monolayers. Interestingly, we should point out that ZZ(Tube) is able to introduce interesting electronic properties into corresponding nanoribbons, for example, all ZZ(Tube) reconstructions open a band gap, and all ZZ(Tube) reconstructions result in a type-II band alignment, making the VBM and CBM charge separated spatially, which are in sharp contrast to metallic ZZ(Pri) edge.

It is noted that here, we focus on the edge reconstruction of freestanding α-puckered monolayers. In real growth conditions, atmospheric species and substrate might influence the edge configuration and reconstruction, which in turn affect the growth kinetics. Previous studies indeed showed that edge reconstruction could affect the growth kinetics of 2D materials, such as graphene,[60-62] phosphorene[63] and MoS_2.[64,65] Clearly, the effects of atmospheric species and substrate on the edge structure and related growth kinetics of α-puckered monolayers deserve further studies. Besides, the atomic fraction during the growth of compound α-puckered monolayers could affect their chemical potential difference, which in turn affects the edge structure and reconstruction. Such phenomenon has been already observed, for example, in graphene,[61] h-BN[66] and MoS_2.[67] Clearly, the effect of the atomic fraction on the edge structure and reconstruction of compound α-puckered monolayers also deserves further studies.

4. Robust type II band structures introducing charge separation spatially

The ZZ(Pri) edge always introduces an edge band crossing the Fermi level as shown in Figure S4a-e.[25,53] However, as shown in Figure 4, the band gaps of ANR, GeSNR, GeSeNR, SnSNR and SnSeNR with ZZ(Tube) are 0.82, 0.99, 0.94, 0.94 and 0.60 eV, respectively. It is noted that our band structures are based on the standard PBE level, which may underestimate the bang gap. However, it is sufficient to predict the correct band type and band gap trend.

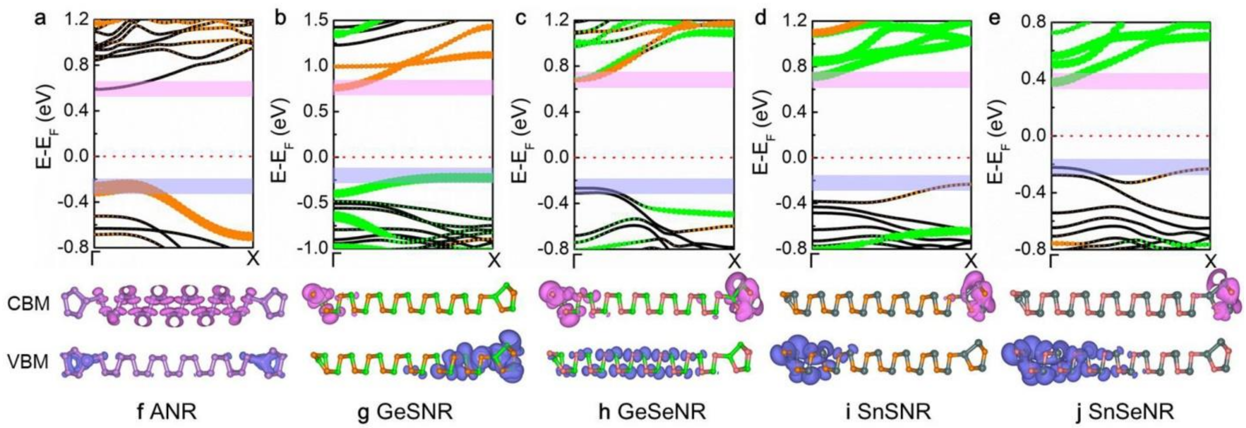

Figure 4. The projected band structures of reconstructed edges of (a) ANR, (b) GeSNR, (c) GeSeNR, (d) SnSNR and (e) SnSeNR, respectively. The projected bands originated from metal edge atoms and nonmetal edge atoms, which are represented by green and orange color circles, respectively. The band decomposed charge density of reconstructed (f) ANR, (g) GeSNR, (h) GeSeNR, (i) SnSNR and (j) SnSeNR, respectively. The isosurface value is set to 2×10^{-5} e/Bohr^3 and 1×10^{-4} e/Bohr^3 for CBM and VBM, respectively.

We then calculated their band decomposed charge density of valence band edge (blue zone in band structures) and conduction band edge (pink zone in band structure). Overall, all the VBM and CBM of reconstructed nanoribbons are separately localized. For ANR (Figure 4a, f), the VBM charge is mainly localized at the ZZ(Tube) edge, while its CBM is originated from inner intrinsic arsenene atoms. For GeSNR, the atoms of ZZ(Ge-Tube) contribute to the valence band edge, while atoms of ZZ(S-R) edge contribute to the CBM charge. For GeSeNR, CBM charge is from both ZZ(Ge-Tube) and ZZ(Se-R), while VBM is from intrinsic inner GeSe monolayer. For SnSNR and SnSeNR, the charge of ZZ(Sn-tube) is always at CBM, while the ZZ(S-R) and ZZ(Se-R) partially contribute to the VBM charge. Although the band structure details for each monolayer are different, the ZZ(Tube) reconstruction always results in a type-II band alignment, where VBM and CBM remain separation spatially. These are beneficial for the separation of photo-generated electrons and holes.[68,69]

5. Charge separation and recombination kinetics by TDDFT

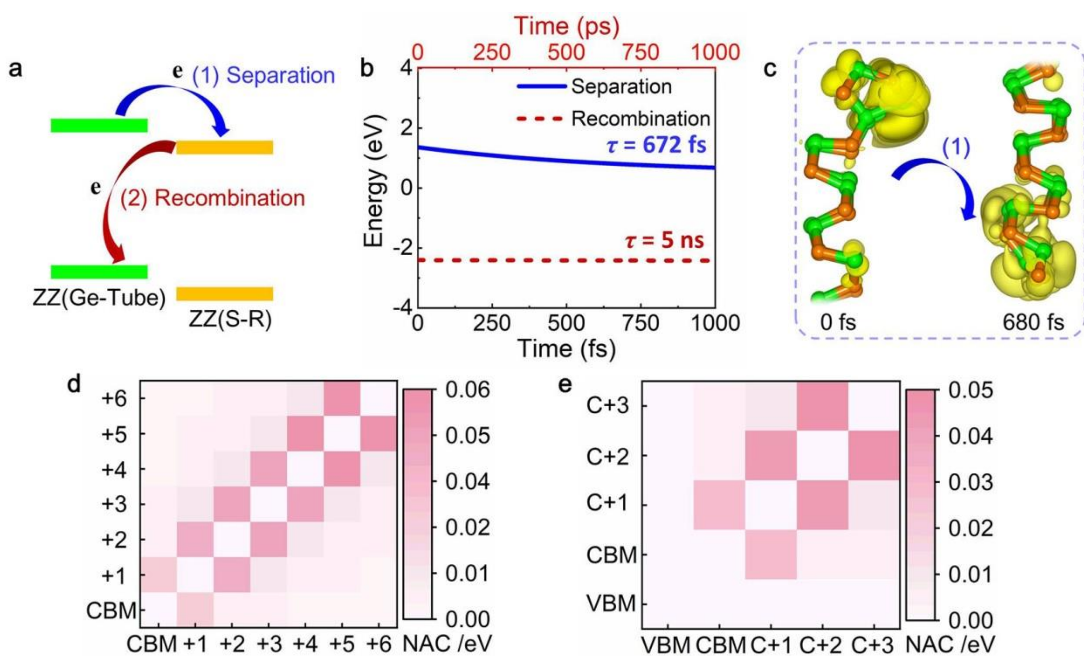

Figure 5. (a) Schematic illustration of electron-hole separation and recombination between the ZZ(Ge-Tube) and ZZ(S-R) edge of GeSNR. (b) Time-dependent energy change of electrons in GeSNR during separation (solid line) and recombination (dash line) from Hefei-NAMD simulations. (c) Snapshots of the orbital distribution of electron densities on GeSNR at 0 fs and 680 fs, corresponding to process (1) in (a). The isosurface value is set to 1×10^{-4} e/Bohr^3. (d, e) Averaged values of nonadiabatic coupling (NAC) between different states near the Fermi level at 300 K. The +1, +2, +3… or C+1, C+2, C+3 denote the CBM+1, CBM+2, CBM+3… of GeSNR.

Beyond, we investigated the photo-generated electron and hole carrier dynamic processes by using the Hefei-NAMD code,[70] which is based on AIMD combining TDDFT and Fewest-Switches Surface Hopping (FSSH) (details can be found in the SI).[71,72] The Hefei-NAMD has been extensively applied in photo-generated carrier simulations and verified by related experimental results.[73-78] A (6×1) supercell with three periodic reconstructed (2×1) edge units was built for the NAMD. The band type is still type-II with VBM at ZZ(Ge-Tube) edge and CBM at the ZZ(S-R) edge, which is the same as above Figure 4b, g.

The key dynamic processes include two parts (Figure 5a): (1) photo-generated electron transfers from ZZ(Ge-Tube) to ZZ(S-R) edge; and (2) photo-generated electron-hole pair recombination. For part (1), the electron will be first excited to CBM (the CBM+6 level of the GeSNR is regarded as the donor level) from VBM at ZZ(Ge-Tube), and then transfer to CBM (the CBM level of the GeSNR is regarded as the acceptor level in NAMD) of ZZ(S-R). We simulated this process by initiating a photo-generated electron localized in the donor state using NAMD at room temperature. Fitting of time-dependent energy (Figure S6a) by $f(t)=A^{*}\exp(-t/\tau)$ (Figure 5b solid line) indicates that the excited electron indeed transfers from the CBM of ZZ(Ge-Tube) to the CBM of ZZ(S-R) within a short period of 672 fs. Within 1 ps, the electron localization on ZZ(S-R) edge increases from 6% to 43% at 300 K (Figure S6b, black line), and both the AD (**ad**iabatic) and NA (**n**on**a**diabatic) mechanisms co-promote the charge transfer (Figure S6b, blue line and red line).

Next, we examined part (2), that is, the recombination process: an electron initially localizes on the CBM of ZZ(S-R) edge, then relaxes to the VBM of ZZ(Ge-Tube) edge. The time-dependent evolution of Kohn-Sham energy states of the reconstructed GeSNR (Figure S8) always exhibits an energy bandgap of 0.38 eV. Therefore, the quantum decoherence must be included. We employed the decoherence-induced surface hopping (DISH) method in this process.[79] The population evolution of electron in ZZ(Ge-Tube) during recombination process increases from 0% to 1.5% within 1 ns with DISH method as shown in Figure S7. Within this approximation, the recombination time is as long as 5 ns by fitting with $f(t)=A^{*}\exp(-t/\tau)$ (Figure 5b, dash line). The recombination time is 4 orders larger than the charge separation time (672 fs). As illustrated in Figure 5c, after 680 fs, the electrons at ZZ(Ge-Tube) quickly transfer to ZZ(S-R). Thus, we conclude that reconstructed GeSNR exhibits ultrafast and robust electron-hole separation.

In the NAMD simulation, the electron transfer probability is determined by the nonadiabatic coupling (NAC) elements, which can be described as:[80]

$$d_{jk}=\left\langle \varphi_j \left| \frac{\partial}{\partial t} \right| \varphi_k \right\rangle = \frac{\langle \varphi_j | \nabla_R H | \varphi_k \rangle}{\varepsilon_k - \varepsilon_j} \dot{R} \qquad (2)$$

where, $\varepsilon_{k/j}$ and $\varphi_{k/j}$ are the eigenvalue and wave functions for the electronic states k and j. H is the Kohn-Sham Hamiltonian. $\dot{R}$ is the velocity of nuclear motion.

Figure 5d visualizes the averaged NAC between different energy states of GeSNR. The NAC between the neighboring states is obviously larger than the separated states. For example, neighboring states NAC[CBM, CBM+1] (0.027 eV) is obviously larger than the separated states NAC[CBM, CBM+2] (0.006 eV), NAC[CBM, CBM+3] (0.004 eV) and NAC[CBM, CBM+4] (0.003 eV). Therefore, electrons are preferred to hop between the neighboring states rather than between the separated states. Beyond, the averaged value of NAC between the VBM and CBM of GeSNR (Figure 5e) is much smaller than that of the electron separation process (Figure 5d). For instance, NAC[VBM, CBM] (1.8×10^{-4} eV) is much smaller than NAC[CBM+1, CBM+2] (0.045 eV), NAC[CBM+2, CBM+3] (0.051 eV). That means that the recombination process is suppressed, which is helpful to achieving effective separation of photo-generated electron-hole pairs.

In addition, Figure S8 shows that the energy difference between donor and acceptor states of the electron transfer process is smaller than that of the recombination process (with bandgap ~0.38 eV), which indicates that a small ε_k-ε_j will increase the value of NAC and promote electron and hole separation efficiently. Besides, the large energy fluctuations of about 0.5 eV between donor and acceptor states of the electron transfer process at 300 K imply a strong electron-phonon coupling. By performing Fourier transform (FT) of the time-dependent evolution of energy states, we obtained the dominant phonon modes coupling with electronic states. For electron separation process, Figure S9a shows that the dominant phonon modes in donor states are 418 cm^{-1}, 318 cm^{-1}, 268 cm^{-1} and 117 cm^{-1} for ZZ(Ge-tube). The 350 cm^{-1} phonon mode at ZZ(S-R) is the dominant acceptor phonon in the separation process, as well as the dominant donor state in the recombination process. In the recombination process, the dominant phonon mode of acceptor state of ZZ(Ge-Tube) locates at 285 cm^{-1} and soft modes are below 150 cm^{-1} (Figure S9b)

It was reported that the high frequency phonon mode (418 cm^{-1}) in the separation process promotes the fast electron transfer, which is crucial for the fast charge spatial separation.[81,82] Previous studies revealed that the highest phonon mode for intrinsic 2D GeS monolayer is far below 400 cm^{-1}.[23,83] Therefore, the high frequency phonon mode of 418 cm^{-1} must originate from the tubed edge.

Conclusions

In summary, we reveal a universal reconstruction for ZZ edge in puckered α-phase puckered monolayers, such as arsenene and group-IV monochalcogenides (GeS/Se and SnS/Se), in which ZZ edge is able to transform into a tubed edge, enabling the ultimate narrow nanotube to terminate the nanoribbons of 2D α-phase puckered monolayers. The lowest-energy structure is verified by the global structure searching package, CALYPSO. Such a tube reconstruction can significantly reduce the edge energy. Furthermore, the reconstruction energy barriers are low, indicating the tube edge is easy to form. After the reconstruction, the structure shows a remarkable stability in

AIMD simulations and phase diagram analyses. Most importantly, this edge reconstruction always induces a robust charge spatial separation between VBM and CBM, which exhibits a type-II band alignment. This remarkable charge spatial separation is confirmed by the TDDFT simulation using the Hefei-NAMD. We further show that the excited electrons of ZZ(Ge-Tube) edge can be separated into the ZZ(S-R) edge in only ~672 fs, while the recombination time is as long as ~5 ns at 300 K. Therefore, the separated charge can accumulate efficiently. The fast charge transfer and slow electron-hole recombination can be explained by the large difference in the averaged values of NAC between the donor and acceptor states. Besides, the ultrafast electron transfer is due to the high frequency phonon mode (418 cm^{-1}), which originates from the tubed edge, suggesting that the unique tubed edge is the true structure for ZZ edge in all α-phase puckered monolayers. The ultrafast charge spatial separation and very slow recombination of the tubed edges are crucial features that are needed for optoelectronic and photocatalytic applications.

Supporting Information. The following files are available free of charge. It includes computational methods, edge formation energy, edge reconstruction process and transition states, band structures, model structure for NAMD simulations, density of state, time dependent energy evolutions, spatial electron localization, population evolution, evolution of energy states, and Fourier transform spectra (PDF)

Corresponding Author

Yong-Wei Zhang – Principal Scientist and Deputy Executive Director, Institute of High Performance Computing, A*STAR, Singapore

Email: zhangyw@ihpc.a-star.edu.sg

Junfeng Gao – Professor, School of Physics, Dalian University of Technology, China

Email: gaojf@dlut.edu.cn

Author

Yanxue Zhang – Key Laboratory of Materials Modification by Laser, Ion and Electron Beams (Dalian University of Technology), Ministry of Education, Dalian 116024, China

Yanyan Zhao – Key Laboratory of Materials Modification by Laser, Ion and Electron Beams (Dalian University of Technology), Ministry of Education, Dalian 116024, China

Yizhen Bai – Key Laboratory of Materials Modification by Laser, Ion and Electron Beams (Dalian University of Technology), Ministry of Education, Dalian 116024, China

Jijun Zhao – Key Laboratory of Materials Modification by Laser, Ion and Electron Beams (Dalian University of Technology), Ministry of Education, Dalian 116024, China; orcid.org/0000-0002-3263-7159

Author Contributions

The manuscript was written through contributions of all authors. All authors have given approval to the final version of the manuscript.

Notes

The authors declare no competing financial interest.

Acknowledgements

This work was supported by the National Natural Science Foundation of China (Grant Nos. 12074053, 91961204, 12004064), the XinLiaoYingCai Project of Liaoning province (XLYC1907163), and the Fundamental Research Funds for the Central Universities of China (DUT21LAB112). This work was partially supported by the National Research Foundation, Singapore, under Award No. NRF-CRP24-2020-0002. We also acknowledge computer support from the Shanghai Supercomputer Center, Tianhe supercomputer of Tianjin center, and DUT supercomputing center.

References

(1) Zhang, S.; Guo, S.; Chen, Z.; Wang, Y.; Gao, H.; Gomez-Herrero, J.; Ares, P.; Zamora, F.; Zhu, Z.; Zeng, H. Recent progress in 2D group-VA semiconductors: from theory to experiment. *Chem. Soc. Rev.* **2018,** *47*, (3), 982-1021.

(2) Hu, Z.; Ding, Y.; Hu, X.; Zhou, W.; Yu, X.; Zhang, S. Recent progress in 2D group IV-IV monochalcogenides: synthesis, properties and applications. *Nanotechnology* **2019,** *30*, (25), 252001.

(3) Mehboudi, M.; Dorio, A. M.; Zhu, W.; van der Zande, A.; Churchill, H. O.; Pacheco-Sanjuan, A. A.; Harriss, E. O.; Kumar, P.; Barraza-Lopez, S. Two-Dimensional Disorder in Black Phosphorus and Monochalcogenide Monolayers. *Nano Lett.* **2016,** *16*, (3), 1704-1712.

(4) Huang, L.; Wu, F.; Li, J. Structural anisotropy results in strain-tunable electronic and optical properties in monolayer GeX and SnX (X = S, Se, Te). *J. Chem. Phys.* **2016,** *144*, (11), 114708.

(5) Fei, R.; Yang, L. Strain-engineering the anisotropic electrical conductance of few-layer black phosphorus. *Nano Lett.* **2014,** *14*, (5), 2884-2889.

(6) Xu, Y.; Xu, K.; Zhang, H. First-Principles Calculations of Angular and Strain Dependence on Effective Masses of Two-Dimensional Phosphorene Analogues (Monolayer alpha-Phase Group-IV Monochalcogenides MX). *Molecules* **2019,** *24*, (3), 639.

(7) Ramasubramaniam, A.; Muniz, A. R. Ab initiostudies of thermodynamic and electronic properties of phosphorene nanoribbons. *Phys. Rev. B* **2014,** *90*, (8), 085424.

(8) Zhao, L. D.; Lo, S. H.; Zhang, Y.; Sun, H.; Tan, G.; Uher, C.; Wolverton, C.; Dravid, V. P.; Kanatzidis, M. G. Ultralow thermal conductivity and high thermoelectric figure of merit in SnSe crystals. *Nature* **2014,** *508*, (7496), 373-377.

(9) Ding, G.; Gao, G.; Yao, K. High-efficient thermoelectric materials: The case of orthorhombic IV-VI compounds. *Sci Rep* **2015,** *5*, 9567.

(10) Shafique, A.; Shin, Y. H. Thermoelectric and phonon transport properties of two-dimensional IV-VI compounds. *Sci Rep* **2017,** *7*, (1), 506.

(11) Fei, R.; Li, W.; Li, J.; Yang, L. Giant piezoelectricity of monolayer group IV monochalcogenides: SnSe, SnS, GeSe, and GeS. *Appl. Phys. Lett.* **2015,** *107*, (17), 173104.

(12) Gomes, L. C.; Carvalho, A.; Castro Neto, A. H. Enhanced piezoelectricity and modified dielectric screening of two-dimensional group-IV monochalcogenides. *Phys. Rev. B* **2015,** *92*, (21), 214103.

(13) Khan, H.; Mahmood, N.; Zavabeti, A.; Elbourne, A.; Rahman, M. A.; Zhang, B. Y.; Krishnamurthi, V.; Atkin, P.; Ghasemian, M. B.; Yang, J.; Zheng, G.; Ravindran, A. R.; Walia, S.; Wang, L.; Russo, S. P.; Daeneke, T.; Li, Y.; Kalantar-Zadeh, K. Liquid metal-based synthesis of high performance monolayer SnS piezoelectric nanogenerators. *Nat. Commun.* **2020,** *11*, (1), 3449.

(14) Fei, R.; Kang, W.; Yang, L. Ferroelectricity and Phase Transitions in Monolayer Group-IV Monochalcogenides. *Phys. Rev. Lett.* **2016,** *117*, (9), 097601.

(15) Chang, K.; Kuster, F.; Miller, B. J.; Ji, J. R.; Zhang, J. L.; Sessi, P.; Barraza-Lopez, S.; Parkin, S. S. P. Microscopic Manipulation of Ferroelectric Domains in SnSe Monolayers at Room Temperature. *Nano Lett.* **2020,** *20*, (9), 6590-6597.

(16) Higashitarumizu, N.; Kawamoto, H.; Lee, C. J.; Lin, B. H.; Chu, F. H.; Yonemori, I.; Nishimura, T.; Wakabayashi, K.; Chang, W. H.; Nagashio, K. Purely in-plane ferroelectricity in monolayer SnS at room temperature. *Nat. Commun.* **2020,** *11*, (1), 2428.

(17) Qiao, J.; Kong, X.; Hu, Z. X.; Yang, F.; Ji, W. High-mobility transport anisotropy and linear dichroism in few-layer black phosphorus. *Nat. Commun.* **2014,** *5*, 4475.

(18) Li, F.; Liu, X.; Wang, Y.; Li, Y. Germanium monosulfide monolayer: a novel two-dimensional semiconductor with a high carrier mobility. *J. Mater. Chem. C* **2016,** *4*, (11), 2155-2159.

(19) Lv, X.; Wei, W.; Sun, Q.; Li, F.; Huang, B.; Dai, Y. Two-dimensional germanium monochalcogenides for photocatalytic water splitting with high carrier mobility. *Appl. Catal. B-Environ.* **2017,** *217*, 275-284.

(20) Xu, L.; Yang, M.; Wang, S. J.; Feng, Y. P. Electronic and optical properties of the monolayer group-IV monochalcogenides MX (M=Ge,Sn; X=S,Se,Te). *Phys. Rev. B* **2017,** *95*, (23), 235434.

(21) Lin, S.; Lai, W. K.; Li, Y.; Lu, W.; Bai, G.; Lau, S. P. Liquid-phase exfoliation of violet phosphorus for electronic applications. *SmartMat* **2021**, 1-8.

(22) Gomes, L. C.; Carvalho, A. Phosphorene analogues: Isoelectronic two-dimensional group-IV monochalcogenides with orthorhombic structure. *Phys. Rev. B* **2015,** *92*, (8), 085406.

(23) Zhang, S.; Wang, N.; Liu, S.; Huang, S.; Zhou, W.; Cai, B.; Xie, M.; Yang, Q.; Chen, X.; Zeng, H. Two-dimensional GeS with tunable electronic properties via external electric field and strain. *Nanotechnology* **2016,** *27*, (27), 274001.

(24) Peng, X.; Wei, Q.; Copple, A. Strain-engineered direct-indirect band gap transition and its mechanism in two-dimensional phosphorene. *Phys. Rev. B* **2014,** *90*, (8), 085402.

(25) Ao, L.; Pham, A.; Xiang, X.; Klose, F.; Li, S.; Zu, X. Tunable electronic and magnetic properties of arsenene nanoribbons. *RSC Adv.* **2017,** *7*, (82), 51935-51943.

(26) Song, X.; Zhou, W.; Liu, X.; Gu, Y.; Zhang, S. Layer-controlled band alignment, work function and optical properties of few-layer GeSe. *Physica B* **2017,** *519*, 90-94.

(27) Xia, F.; Wang, H.; Xiao, D.; Dubey, M.; Ramasubramaniam, A. Two-dimensional material nanophotonics. *Nat. Photonics* **2014,** *8*, (12), 899-907.

(28) Lan, C.; Li, C.; Yin, Y.; Guo, H.; Wang, S. Synthesis of single-crystalline GeS nanoribbons for high sensitivity visible-light photodetectors. *J. Mater. Chem. C* **2015,** *3*, (31), 8074-8079.

(29) Ramasamy, P.; Kwak, D.; Lim, D.-H.; Ra, H.-S.; Lee, J.-S. Solution synthesis of GeS and GeSe nanosheets for high-sensitivity photodetectors. *J. Mater. Chem. C* **2016,** *4*, (3), 479-485.

(30) Michael, G.; Hu, G.; Zheng, D.; Zhang, Y. Piezo-phototronic solar cell based on 2D monochalcogenides materials. *J. Phys. D: Appl. Phys.* **2019,** *52*, (20), 204001.

(31) Wang, B.; Zhong, S. P.; Zhang, Z. B.; Zheng, Z. Q.; Zhang, Y. P.; Zhang, H. Broadband photodetectors based on 2D group IVA metal chalcogenides semiconductors. *Appl. Mater. Today* **2019,** *15*, 115-138.

(32) Sutter, E.; Zhang, B.; Sun, M.; Sutter, P. Few-Layer to Multilayer Germanium(II) Sulfide: Synthesis, Structure, Stability, and Optoelectronics. *ACS Nano* **2019,** *13*, (8), 9352-9362.

(33) Kushnir, K.; Wang, M.; Fitzgerald, P. D.; Koski, K. J.; Titova, L. V. Ultrafast Zero-Bias Photocurrent in GeS Nanosheets: Promise for Photovoltaics. *ACS Energy Lett.* **2017,** *2*, (6), 1429-1434.

(34) Zhang, X.; Xin, J.; Ding, F. The edges of graphene. *Nanoscale* **2013,** *5*, (7), 2556-2569.

(35) Qi, H.; Liang, B.; Kaiser, U. Perspective towards atomic-resolution imaging of two-dimensional polymers. *SmartMat* **2021**, 1-8.

(36) Koskinen, P.; Malola, S.; Hakkinen, H. Self-passivating edge reconstructions of graphene. *Phys. Rev. Lett.* **2008,** *101*, (11), 115502.

(37) Koskinen, P.; Malola, S.; Häkkinen, H. Evidence for graphene edges beyond zigzag and armchair. *Phys. Rev. B* **2009,** *80*, (7), 073401.

(38) Gao, J.; Liu, X.; Zhang, G.; Zhang, Y. W. Nanotube-terminated zigzag edges of phosphorene formed by self-rolling reconstruction. *Nanoscale* **2016,** *8*, (41), 17940-17946.

(39) Cui, P.; Choi, J. H.; Chen, W.; Zeng, J.; Shih, C. K.; Li, Z.; Zhang, Z. Contrasting Structural Reconstructions, Electronic Properties, and Magnetic Orderings along Different Edges of Zigzag Transition Metal Dichalcogenide Nanoribbons. *Nano Lett.* **2017,** *17*, (2), 1097-1101.

(40) Wang, N.; Cao, D.; Wang, J.; Liang, P.; Chen, X.; Shu, H. Semiconducting edges and flake-shape evolution of monolayer GaSe: role of edge reconstructions. *Nanoscale* **2018,** *10*, (25), 12133-12140.

(41) Kim, K.; Coh, S.; Kisielowski, C.; Crommie, M. F.; Louie, S. G.; Cohen, M. L.; Zettl, A. Atomically perfect torn graphene edges and their reversible reconstruction. *Nat. Commun.* **2013,** *4*, 2723.

(42) Liu, Z.; Lin, Y. C.; Lu, C. C.; Yeh, C. H.; Chiu, P. W.; Iijima, S.; Suenaga, K. In situ observation of step-edge in-plane growth of graphene in a STEM. *Nat. Commun.* **2014,** *5*, 4055.

(43) He, K.; Robertson, A. W.; Fan, Y.; Allen, C. S.; Lin, Y.-C.; Suenaga, K.; Kirkland, A. I.; Warner, J. H. Temperature dependence of the reconstruction of zigzag edges in graphene. *ACS nano* **2015,** *9*, (5), 4786-4795.

(44) Hyun, C.; Yun, J.; Cho, W. J.; Myung, C. W.; Park, J.; Lee, G.; Lee, Z.; Kim, K.; Kim, K. S. Graphene edges and beyond: temperature-driven structures and electromagnetic properties. *ACS nano* **2015,** *9*, (5), 4669-4674.

(45) Deng, Q.; Zhao, J. Triggering One-Dimensional Phase Transition with Defects at the Graphene Zigzag Edge. *Nano Lett.* **2016,** *16*, (2), 1244-1249.

(46) Li, D.; Wang, Y.; Cui, T.; Ma, Y.; Ding, F. Local Carbon Concentration Determines the Graphene Edge Structure. *J Phys Chem Lett* **2020,** *11*, (9), 3451-3457.

(47) Chen, Y.; Cui, P.; Ren, X.; Zhang, C.; Jin, C.; Zhang, Z.; Shih, C. K. Fabrication of MoSe2 nanoribbons via an unusual morphological phase transition. *Nat. Commun.* **2017,** *8*, 15135.

(48) Son, Y. W.; Cohen, M. L.; Louie, S. G. Half-metallic graphene nanoribbons. *Nature* **2006,** *444*, (7117), 347-349.

(49) Ding, L. P.; Ding, F. Self-passivation leads to semiconducting edges of black phosphorene. *Nanoscale Horiz.* **2021,** *6*, (2), 148-155.

(50) Liu, Y.; Li, D.; Cui, T. Edge reconstructions of black phosphorene: a global search. *Nanoscale* **2021,** *13*, (7), 4085-4091.

(51) Liu, X.; Gao, J.; Zhang, G.; Zhang, Y. W. Unusual Twisting Phonons and Breathing Modes in Tube-Terminated Phosphorene Nanoribbons and Their Effects on Thermal Conductivity. *Adv. Funct. Mater.* **2017,** *27*, (48), 1702776.

(52) Kamal, C.; Ezawa, M. Arsenene: Two-dimensional buckled and puckered honeycomb arsenic systems. *Phys. Rev. B* **2015,** *91*, (8), 085423.

(53) Li, R.; Cao, H.; Dong, J. Electronic properties of group-IV monochalcogenide nanoribbons: Studied from first-principles calculations. *Phys. Lett. A* **2017,** *381*, (44), 3747-3753.

(54) Wang, Y.; Lv, J.; Zhu, L.; Ma, Y. Crystal structure prediction via particle-swarm optimization. *Phys. Rev. B* **2010,** *82*, (9), 094116.

(55) Wang, Y.; Lv, J.; Zhu, L.; Lu, S.; Yin, K.; Li, Q.; Wang, H.; Zhang, L.; Ma, Y. Materials discovery via CALYPSO methodology. *J. Phys. Condens. Matter* **2015,** *27*, (20), 203203.

(56) Wang, H.; Wang, Y.; Lv, J.; Li, Q.; Zhang, L.; Ma, Y. CALYPSO structure prediction method and its wide application. *Comput. Mater. Sci.* **2016,** *112*, 406-415.

(57) Pumera, M.; Wong, C. H. Graphane and hydrogenated graphene. *Chem. Soc. Rev.* **2013,** *42*, (14), 5987-5995.

(58) Wassmann, T.; Seitsonen, A. P.; Saitta, A. M.; Lazzeri, M.; Mauri, F. Structure, stability, edge states, and aromaticity of graphene ribbons. *Phys. Rev. Lett.* **2008,** *101*, (9), 096402.

(59) Chase Jr, M. W. NIST-JANAF thermochemical tables. *J. Phys. Chem. Ref. Data, Monograph 9* **1998,** *9*, 1-1951.

(60) Shu, H.; Chen, X.; Ding, F. The edge termination controlled kinetics in graphene chemical vapor deposition growth. Chem. Sci. 2014, 5, (12), 4639-4645.

(61) Gao, J.; Zhao, J.; Ding, F. Transition Metal Surface Passivation Induced Graphene Edge Reconstruction. J. Am. Chem. Soc. 2012, 134, (14), 6204-6209.

(62) Chen, Y.; Sun, J.; Gao, J.; Du, F.; Han, Q.; Nie, Y.; Chen, Z.; Bachmatiuk, A.; Priydarshi, M. K.; Ma, D.; Song, X.; Wu, X.; Xiong, C.; Rummeli, M. H.; Ding, F.; Zhang, Y.; Liu, Z. Growing Uniform Graphene Disks and Films on Molten Glass for Heating Devices and Cell Culture. Adv. Mater. 2015, 27, (47), 7839-7846.

(63) Gao, J.; Zhang, G.; Zhang, Y. W. The Critical Role of Substrate in Stabilizing Phosphorene Nanoflake: A Theoretical Exploration. J. Am. Chem. Soc. 2016, 138, (14), 4763-4771.

(64) Lauritsen, J. V.; Kibsgaard, J.; Helveg, S.; Topsoe, H.; Clausen, B. S.; Laegsgaard, E.; Besenbacher, F. Size-dependent structure of MoS2 nanocrystals. Nat Nanotechnol 2007, 2, (1), 53-58.

(65) Zhao, X.; Fu, D.; Ding, Z.; Zhang, Y. Y.; Wan, D.; Tan, S. J. R.; Chen, Z.; Leng, K.; Dan, J.; Fu, W.; Geng, D.; Song, P.; Du, Y.; Venkatesan, T.; Pantelides, S. T.; Pennycook, S. J.; Zhou, W.; Loh, K. P. Mo-Terminated Edge Reconstructions in Nanoporous Molybdenum Disulfide Film. Nano Lett. 2018, 18, (1), 482-490.

(66) Liu, Y.; Bhowmick, S.; Yakobson, B. I. BN white graphene with "colorful" edges: the energies and morphology. Nano Lett. 2011, 11, (8), 3113-3116.

(67) Cao, D.; Shen, T.; Liang, P.; Chen, X.; Shu, H. Role of Chemical Potential in Flake Shape and Edge Properties of Monolayer MoS2. J. Phys. Chem. C 2015, 119, (8), 4294-4301.

(68) Lo, S. S.; Mirkovic, T.; Chuang, C.-H.; Burda, C.; Scholes, G. D. Emergent Properties Resulting from Type-II Band Alignment in Semiconductor Nanoheterostructures. *Adv. Mater.* **2011,** *23*, (2), 180-197.

(69) Fang, M.-J.; Tsao, C.-W.; Hsu, Y.-J. Semiconductor nanoheterostructures for photoconversion applications. *J. Phys. D* **2020,** *53*, (14), 143001.

(70) Zheng, Q.; Chu, W.; Zhao, C.; Zhang, L.; Guo, H.; Wang, Y.; Jiang, X.; Zhao, J. Ab initio nonadiabatic molecular dynamics investigations on the excited carriers in condensed matter systems. *Wiley Interdiscip. Rev.-Comput. Mol. Sci.* **2019,** *9*, (6), 1-27.

(71) Craig, C. F.; Duncan, W. R.; Prezhdo, O. V. Trajectory surface hopping in the time-dependent Kohn-Sham approach for electron-nuclear dynamics. *Phys. Rev. Lett.* **2005,** *95*, (16), 163001.

(72) Akimov, A. V.; Prezhdo, O. V. Advanced Capabilities of the PYXAID Program: Integration Schemes, Decoherence Effects, Multiexcitonic States, and Field-Matter Interaction. *J. Chem. Theory Comput.* **2014,** *10*, (2), 789-804.

(73) Weibin Chu, Q. Z., Oleg V. Prezhdo, Jin Zhao, Wissam A. Saidi. Low-frequency lattice phonons in halide perovskites explain high defect tolerance toward electron-hole recombination. Sci. Adv. 6, (7), 8.

(74) Weibin Chu, W. A. S., Jin Zhao,and Oleg V. Prezhdo. Soft Lattice and Defect Covalency Rationalize Tolerance of b-CsPbI3 Perovskite Solar Cells to Native Defects. Angew. Chem.-Int. Edit. 59, (16), 6435-6441.

(75) Xiang Jiang, Q. Z., Zhenggang Lan, Wissam A. Saidi, Xinguo Ren, Jin Zhao. Real-time GW-BSE investigations on spin-valley exciton dynamics in monolayer transition metal dichalcogenide. Sci. Adv. 7, (10), 9.

(76) Chen, C.; Kong, L.; Wang, Y.; Cheng, P.; Feng, B.; Zheng, Q.; Zhao, J.; Chen, L.; Wu, K. Dynamics of Single-Molecule Dissociation by Selective Excitation of Molecular Phonons. Phys. Rev. Lett. 2019, 123, (24), 246804.

(77) Chu, W.; Zheng, Q.; Prezhdo, O. V.; Zhao, J. CO2 Photoreduction on Metal Oxide Surface Is Driven by Transient Capture of Hot Electrons: Ab Initio Quantum Dynamics Simulation. J. Am. Chem. Soc. 2020, 142, (6), 3214-3221.

(78) Ni, K.; Du, J.; Yang, J.; Xu, S.; Cong, X.; Shu, N.; Zhang, K.; Wang, A.; Wang, F.; Ge, L.; Zhao, J.; Qu, Y.; Novoselov, K. S.; Tan, P.; Su, F.; Zhu, Y. Stronger Interlayer Interactions Contribute to Faster Hot Carrier Cooling of Bilayer Graphene under Pressure. Phys. Rev. Lett. 2021, 126, (2), 027402.

(79) Jaeger, H. M.; Fischer, S.; Prezhdo, O. V. Decoherence-induced surface hopping. *J. Chem. Phys.* **2012,** *137*, (22), 22A545.

(80) Wong, J. C.; Li, L.; Kanai, Y. Size Dependence and Role of Decoherence in Hot Electron Relaxation within Fluorinated Silicon Quantum Dots: A First-Principles Study. *J. Phys. Chem. C* **2018,** *122*, (51), 29526-29536.

(81) Niu, X.; Li, Y.; Zhang, Y.; Zheng, Q.; Zhao, J.; Wang, J. Highly efficient photogenerated electron transfer at a black phosphorus/indium selenide heterostructure interface from ultrafast dynamics. *J. Mater. Chem. C* **2019,** *7*, (7), 1864-1870.

(82) Yu, X.; Su, Y.; Xu, W. W.; Zhao, J. Efficient Photoexcited Charge Separation at the Interface of a Novel 0D/2D Heterojunction: A Time-Dependent Ultrafast Dynamic Study. *J. Phys. Chem. Lett.* **2021,** *12*, (9), 2312-2319.

(83) Qin, G.; Qin, Z.; Fang, W. Z.; Zhang, L. C.; Yue, S. Y.; Yan, Q. B.; Hu, M.; Su, G. Diverse anisotropy of phonon transport in two-dimensional group IV-VI compounds: A comparative study. *Nanoscale* **2016,** *8*, (21), 11306-11319.

TOC

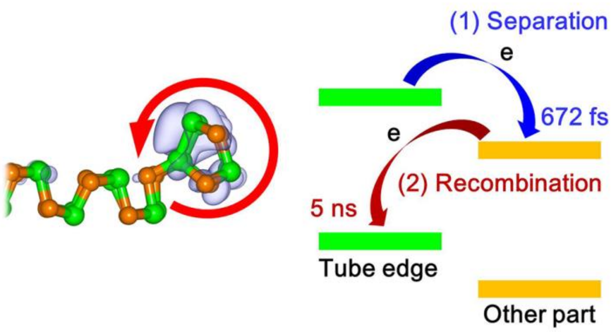

For TOC only